Asociación Argentina
de Mecánica Computacional

Mecánica Computacional Vol XXIX, págs. 1203-1224 (artículo completo)
Eduardo Dvorkin, Marcela Goldschmit, Mario Storti (Eds.)
Buenos Aires, Argentina, 15-18 Noviembre 2010

NON-LINEAR DYNAMIC RESPONSE OF A ROTATING THIN-WALLED COMPOSITE BEAM

Sebastián P. Machado[a,b] **and Cesar M. Saravia**[a,b]

[a]*Grupo Análisis de Sistemas Mecánicos, Centro de Investigaciones de Mecánica Teórica y Aplicada, Universidad Tecnológica Nacional FRBB. 11 de Abril 461, B8000LMI, Bahía Blanca. Argentina*
smachado@frbb.utn.edu.ar, msaravia@frbb.utn.edu.ar

[b]*Consejo Nacional de Investigaciones Científicas y Tecnológicas. Argentina*

Keywords: Composite material, thin-walled rotating beam, non-linear dynamic.

Abstract. The nonlinear planar response of a cantilever rotating slender beam to a principal parametric resonance of its first bending mode is analyzed. The equation of motion is obtained in the form of an integro-partial differential equation, taking into account mid-plane stretching, a rotation speed and modal damping. A composite linear elastic material is considered and the cross-section properties are assumed to be constant given the assumption of small strains. The beam is subjected to a harmonic transverse load in the presence of internal resonance. The internal resonance can be activated for a range of the beam rotating speed, where the second natural frequency is approximately three times the first natural frequency. The method of multiple scales method is used to derive four-first ordinary differential equations that govern the evolution of the amplitude and phase of the response. These equations are used to determine the steady state responses and their stability. Amplitude and phase modulation equations as well as external force–response and frequency–response curves are obtained. Numerical simulations show a complex dynamic scenario and detect chaos and unbounded motions in the instability regions of the periodic solutions.

1 INTRODUCTION

Vibrations of rotating blades or beams have been a subject of constant research interest since they are applied in the design of helicopter blades, turbopropeller blades, wind-turbine blades and robotic arms. The most simplified representation of a rotating beam is a one-dimensional Euler-Bernoulli model. A uniform rotating beam of doubly symmetric cross-section is a special case (no torsional motion: i.e., out-of-plane (flapping) vibration and in-plane (lead-lag) vibration are uncoupled). Owing to the stiffening effect of the centrifugal tension, one can expect the natural frequencies to increase with an increase in the speed of rotation. In several publications a cantilever beam under rotating speed has been considered and approximate methods such as Rayleigh-Ritz, Galerkin, finite element methods, etc., has been used to derive natural frequencies (Schilhansl, 1958; Wang et al. 1976; Leissa, 1981; Hodges and Rutkowski, 1981). However, the nonlinear dynamic analysis of rotating beam is rather rare in the literature (Pesheck et al. 2002a and b; Apiwattanalunggarn et al. 2003; Turhan and Bulut, 2009). Systematic procedures have been developed to obtain reduced-order models (ROMs) via nonlinear normal modes (NNMs) that are based on invariant manifolds in the state space of nonlinear systems (Shaw and Pierre 1993, 1994; Shaw et al., 1999). These procedures initially used asymptotic series to approximate the geometry of the invariant manifold and have been used to study the nonlinear rotating Euler–Bernoulli beam (Pesheck et al., 2002a). Pesheck et al. 2002b, employed a numerically-based Galerkin approach to obtain the geometry of the NNM invariant manifolds out to large amplitudes. These procedures can be applied to more general nonlinearities over wider amplitude ranges, and have been applied to study the vibrations of a rotating Euler–Bernoulli beam (Pesheck et al., 2001). Apiwattanalunggarn et al. (2003) presented a nonlinear one-dimensional finite-element model representing the axial and transverse motions of a cantilevered rotating beam, which is reduced to a single nonlinear normal mode using invariant manifold techniques. They used their approach to study the dynamic characteristics of the finite element model over a wide range of vibration amplitudes. As it can be note, the interest of most of works about nonlinear dynamic of rotating beams are focus on the reduced-order model as the invariant manifold solution. Turhan and Bulut (2009) investigated the in plane nonlinear vibrations of a rotating beam via single- and two-degree-of-freedom models obtained through Galerkin discretization. They performed a perturbation analyses on single- and two-degree-of-freedom models to obtain amplitude dependent natural frequencies and frequency responses. In the last four references, the computational cost associated with generating the manifold solution and the efficiency of the resultant model was mainly analyzed.

From the review of literature, it is found that the study of internal resonance in the area of cantilever rotating slender beam subjected to a harmonic transverse load has not yet been explored so far. The nonlinear modal interaction or the internal resonance in the system arising out of commensurable relationships of frequencies, in presence of parametric excitation due to periodic load can have possible influence on system behavior, which needs to be studied.

In the present paper, we analyze the nonlinear planar vibration of a rotating cantilever beam with harmonic transverse load in the presence of internal resonance. The model is based on one-dimensional Euler-Bernoulli formulation where the geometric cubic nonlinear terms are included in the equation of motion due to midline stretching of the beam. The linear frequencies of the system are dependent on the rotation speed and this effect is used to activate the internal resonance. For a particular rotation speed the second natural frequency is approximately three times the first natural frequency and hence the first and second modes may interact due to a three-one internal resonance. Principal parametric resonance of first

mode considering internal resonance is analyzed here. Principal parametric resonance of second mode in presence of 3:1 internal resonance is not considered here due to lack of space and is studied in another paper. For a comprehensive review of nonlinear modal interactions, we refer the reader to Nayfeh and Mook (1979), Nayfeh and Balachandran (1989), and Nayfeh (1996).

The method of multiple scales (MMS) is used to attack directly the governing nonlinear partial differential equation of motion of the beam and reduced the problem to sets of first-order nonlinear modulation equations in terms of the complex modes of the beam. These modulation equations are numerically analyzed for stability and bifurcations of trivial and nontrivial solutions. Bifurcation diagrams representing system responses with variation of parameters like amplitude and frequency of the lateral excitation load, frequency detuning of internal resonances and damping are computed with the help of a continuation algorithm (Nayfeh and Balachandran, 1995). The trivial state stability plots are presented. The modulation equations are also numerically integrated to obtain the dynamic solutions periodic, quasiperiodic and chaotic responses for typical system parameters.

For the principal parametric resonance of first mode, the influence of internal resonance is illustrated in the frequency and amplitude responses. The system is shown to have Hopf bifurcations and saddle node bifurcations for different parameter values. The influence of intensity of transverse load amplitude and frequency detuning for internal resonance on the strength of nonlinear modal interaction are illustrated. The system is shown to exhibit dynamic solutions like periodic and quasiperiodic responses for typical range of parameter values.

2. NON-LINEAR EQUATIONS OF MOTION

We consider the dynamic response of a rotating box beam subjected to harmonic transverse loads (see Figure 1). The origin of the beam coordinate system (x, y, z) is located at the blade root at an offset R_0 from the rotation axis fixed in space. R_0 denotes the radius of the hub (considered to be rigid) in which the blade or beam is mounted and which rotates about its polar axis through the origin *0*. We assume that the motion is planar and the cross sections remains plane during transverse bending. The laminate stacking sequence is assumed to be symmetric and balanced (Barbero, 1999). A doubly symmetric cross-section box-beam is used and so out-of-plane (flapping) and in-plane (lead-lag) vibration are uncoupled. Neglecting rotary inertia and the transverse shear, the non-linear equations of motion of a rotating beam yields (Machado et al. 2007; Librescu, 2006):

$$\rho A\, \ddot{u} - N' - \rho A\left(R_0 + x + u\right)\Omega^2 = 0\,, \tag{1}$$

$$EI\, v^{iv} - \left(N\, v'\right)' + \rho A\, \ddot{v} = F(x)\cos(\varpi t)\,, \tag{2}$$

where N is axial beam force,

$$N = EA\left(u' + \frac{1}{2}v'^2\right), \tag{3}$$

Ω is the beam rotation speed, ρA is the mass per unit length, EA and EI are the axial and flexural rigidity, ϖ is the excitation frequency, and $F(x)$ describes the spatial distribution of the applied transverse harmonic load. Overdots indicate differentiation with respect to time and primes with respect to the axial co-ordinate.

If the inertial effects along the longitudinal direction are neglected and considering the radius

of the hub $R_0 = 0$, by the direct integration the Eq. (1) in conjunction with the boundary condition of zero axial load at the free end, then

$$N = -\rho A\Omega^2 \frac{x^2}{2} + cte. \tag{4}$$

Substituting Eq. (3) into Eq. (4), one obtains

$$u' + \frac{1}{2}v'^2 + \frac{\rho A}{EA}\,\Omega^2 \frac{x^2}{2} - cte = 0\,, \tag{5}$$

where the integration constant denoted as $\varepsilon_0(t)$ can be evaluated by taking the average value on both sides of Eq. (5) along the beam length L:

$$\varepsilon_0(t) = \frac{u_L - u_0}{L} + \frac{1}{2L}\int_0^L v'^2 \mathrm{dx} + \frac{\rho A}{6EA}\,\Omega^2 L^2\,, \tag{6}$$

Substituting Eq. (3) into Eq. (2) and then from Eqs. (5) and (6) for u' and from the differenced Eq. (4) for u'' in the modified Eq. (2), the following equation of transversal motion yields:

$$\rho A\,\ddot{v} + EI\,v^{iv} - EA\left[\frac{u_L - u_0}{L} + \frac{1}{2L}\int_0^L v'^2 \mathrm{dx} + \frac{\Omega^2 \rho A}{2EA}\left(\frac{L^2}{3} - x^2\right)\right]v'' + \rho A\Omega^2 v' x = F(x)\cos(\varpi t)\,. \tag{7}$$

In this case, for a rotating cantilever beam, supposing that the left end is fixed, that is, $u_0 = 0$, from Eq. (5) the axial force along the bean length for any time is

$$\begin{aligned} N(x,t) &= EA\varepsilon_0(t) - \rho A\Omega^2 \frac{x^2}{2} \\ &= \frac{EAu_L}{L} + \frac{\rho A}{2}\,\Omega^2\left(\frac{L^2}{3} - x^2\right) + \frac{EA}{2L}\int_0^L v'^2 \mathrm{dx}. \end{aligned} \tag{8}$$

Taking Eq. (8) into consideration, Eq. (7) can be concisely rewritten as

$$\rho A\,\ddot{v} + EI\,v^{iv} - N(x,t)v'' + \rho A\Omega^2 v' x = F(x)\cos(\varpi t)\,. \tag{9}$$

To eliminate the spatial dependence we introduce an approximation in Eq. (9) considering the average value of the axial and centrifugal force along the beam:

$$\rho A\,\ddot{v} + EI\,v^{iv} - \bar{N}v'' - \frac{EA}{2L}v''\int_0^L v'^2 \mathrm{dx} + \rho A\Omega^2 v' \frac{L}{2} = F(x)\cos(\varpi t)\,. \tag{10}$$

Notice that

$$\bar{N} = N_0(0) - \frac{\rho A}{6}\,\Omega^2 L^2 = \frac{EA}{L}u_L\,, \tag{11}$$

where $N_0(0)$ is the tensile axial force applied to the originally rectilinear beam at its right end in time $t = 0$.

$$N_0(0) = \frac{EA}{L}u_L + \frac{\rho A}{6}\,\Omega^2 L^2\,. \tag{12}$$

On the other hand, the cantilever boundary conditions demand that

$$\begin{aligned} v = 0 \quad &\text{and} \quad v' = 0 \quad \text{at } x = 0, \\ v'' = 0 \quad &\text{and} \quad v''' = 0 \quad \text{at } x = L. \end{aligned} \tag{13}$$

Finally, introducing a nondimensional quantity for $x^* = x / L$, substituting this relationship in Eqs. (10) and (13), adding damping μ, and dropping the asterisk the expressions can be conveniently rewritten as

$$\ddot{v} + \alpha v^{iv} + 2\mu\dot{v} - \chi v'' - \gamma v'' \int_0^1 v'^2 \mathrm{dx} + \lambda v' = f\cos(\varpi t), \tag{14}$$

$$\begin{aligned} v = 0 \quad &\text{and} \quad v' = 0 \quad \text{at } x = 0, \\ v'' = 0 \quad &\text{and} \quad v''' = 0 \quad \text{at } x = 1, \end{aligned} \tag{15}$$

where

$$\alpha = \frac{EI}{\rho A L^4}, \quad \chi = \frac{\bar{N}}{\rho A L^2}, \quad \gamma = \frac{EA}{2\rho A L^4}, \quad \lambda = \frac{\Omega^2}{2}, \quad f = \frac{F(x)}{\rho A}. \tag{16}$$

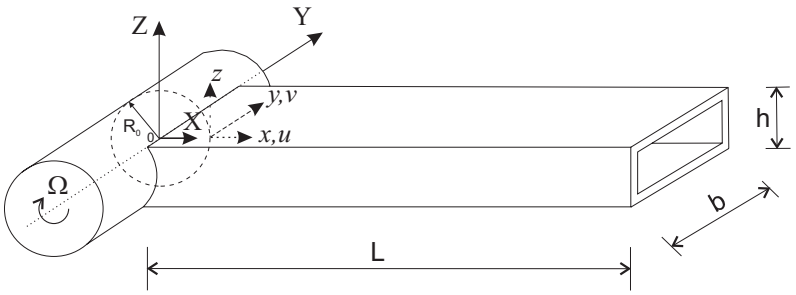

Figure 1. A schematic description of the rotating box beam.

2 METHOD OF ANALISIS

The present system of rotating cantilever beam is analyzed in the form of a first-order uniform expansion through the MMS applied directly to the partial differential Eq. (14) and the associated boundary conditions Eq. (15). The direct perturbation technique has been used considering its advantage over the discretization perturbation technique (Nayfeh el al. 1992; Nayfeh, 1996). Though the direct perturbation method and the discretization-perturbation method, both for linear and nonlinear systems, yield identical results for infinite modes, the former gives better results for finite mode truncation if a higher order perturbation scheme were used. For lower order perturbation schemes, as adopted in the present case, both methods yield identical results. But the choice of orthogonal basis functions for the discretization-perturbation equation might not be so straightforward for some involved cases and a transformation of equation to a convenient form for orthogonalizing the modes may be needed. In such a case, employing the direct perturbation method would be more straightforward, even though the algebra might be more involved.

We seek an approximate solution to this weakly nonlinear distributed parameter system in the form of a first-order uniform expansion and introduce the time scale $T_n = \varepsilon^n t$, $n = 0,1,2,...$ The time derivatives are

$$\frac{d}{dt} = D_0 + \varepsilon D_1 + ..., \quad \frac{d^2}{dt^2} = D_0^2 + 2\varepsilon D_0 D_1 + ..., D_n = \frac{\partial}{\partial T_n}, \quad n = 0,1,2,.... \tag{17}$$

A small parameter ε is introduced by ordering the linear damping and load amplitude as $\mu = \varepsilon\tilde{\mu}, f = \varepsilon\tilde{f}$. Moreover, the displacement $v(x,t)$ are expanded as:

$$v(x,t) = v_1(T_0, T_1, x) + \varepsilon\, v_2(T_0, T_1, x) + ... \tag{18}$$

Substituting Eqs. (17) and (18) into Eqs. (14) and (15) and equating coefficients of like powers of ε on both sides, we obtain

Order ε^0 :

$$D_0^2 v_1 + \alpha v_1^{iv} - \chi v_1'' + \lambda v_1' = 0 \tag{19}$$

$$v_1 = 0, \quad v_1' = 0 \quad \text{at } x = 0, \tag{20}$$

$$v_1'' = 0, \quad v_1''' = 0 \quad \text{at } x = 1. \tag{21}$$

Order ε^1 :

$$D_0^2 v_2 + \alpha v_2^{iv} - \chi v_2'' + \lambda v_2' = -2D_0 D_1 v_1 - 2\mu(x) D_0 v_1 - \gamma v_1'' \int_0^1 v_1'^2 \mathrm{dx} + f\cos(\varpi t) \tag{22}$$

$$v_2 = 0, \quad v_2' = 0 \quad \text{at } x = 0, \tag{23}$$

$$v_2'' = 0, \quad v_2''' = 0 \quad \text{at } x = 1. \tag{24}$$

The solution to the first-order perturbation Eqs. (19-21) can be expressed as

$$v_1(T_0, T_1, x) = \sum_{m=1}^{\infty} \phi_m(x) A_m(T_1) e^{\mathrm{i}\omega_m T_0} + cc, \tag{25}$$

where $\phi_m(x)$ are the mode shapes, ω_m are the natural frequencies and cc stands for complex conjugate. The mode shapes $\phi_m(x)$ for the specified cantilever boundary conditions are calculated as

$$\begin{aligned}\phi_m(x) = e^{x\beta_{4m}} + \Big\{ & e^{x\beta_{3m}} \left[-e^{\beta_{2m}} \beta_{2m}^2 (\beta_{1m} - \beta_{4m}) + e^{\beta_{1m}} \beta_{1m}^2 (\beta_{2m} - \beta_{4m}) + e^{\beta_{4m}} \beta_{4m}^2 (\beta_{1m} - \beta_{2m}) \right] \\ & + e^{x\beta_{2m}} \left[e^{\beta_{3m}} \beta_{3m}^2 (\beta_{1m} - \beta_{4m}) - e^{\beta_{1m}} \beta_{1m}^2 (\beta_{3m} - \beta_{4m}) - e^{\beta_{4m}} \beta_{4m}^2 (\beta_{1m} - \beta_{3m}) \right] \\ & + e^{x\beta_{1m}} \left[-e^{\beta_{3m}} \beta_{3m}^2 (\beta_{2m} - \beta_{4m}) + e^{\beta_{2m}} \beta_{2m}^2 (\beta_{3m} - \beta_{4m}) + e^{\beta_{4m}} \beta_{4m}^2 (\beta_{2m} - \beta_{3m}) \right] \Big\} \Big/ \Big[-e^{\beta_{2m}} \beta_{2m}^2 \\ & (\beta_{1m} - \beta_{3m}) + e^{\beta_{1m}} \beta_{1m}^2 (\beta_{2m} - \beta_{3m}) + e^{\beta_{3m}} \beta_{3m}^2 (\beta_{1m} - \beta_{2m}) \Big]\end{aligned} \tag{26}$$

where β_{im} are the eigenvalues which satisfy the relation

$$\alpha\beta_{im}^4 - \chi\beta_{im}^2 + \lambda\beta_{im} - \omega_m^2 = 0, \qquad i = 1,2,3,4 \tag{27}$$

and the characteristic equation

$$
\begin{aligned}
&(\beta_{2n}-\beta_{3n})(\beta_{1m}-\beta_{4m})\left(e^{\beta_{2n}+\beta_{3n}}\beta_{2n}^2\beta_{3n}^2+e^{\beta_{1n}+\beta_{4n}}\beta_{1n}^2\beta_{4n}^2\right)\\
&+(\beta_{1n}-\beta_{3n})(\beta_{2m}-\beta_{4m})\left(-e^{\beta_{1n}+\beta_{3n}}\beta_{1n}^2\beta_{3n}^2-e^{\beta_{2n}+\beta_{4n}}\beta_{2n}^2\beta_{4n}^2\right)\\
&+(\beta_{1n}-\beta_{2n})(\beta_{3m}-\beta_{4m})\left(e^{\beta_{1n}+\beta_{2n}}\beta_{1n}^2\beta_{2n}^2+e^{\beta_{3n}+\beta_{4n}}\beta_{3n}^2\beta_{4n}^2\right)=0.
\end{aligned}
\tag{28}
$$

The linear natural frequencies of the cantilever beam vary with the rotation speed for different modes for variation of parameters like flexural stiffness and beam mass. For specific combinations of system parameters, the lower natural frequencies can be commensurable, leading to internal resonance in the system and nonlinear interaction between the associated modes. We analyze the specific case of two mode interaction corresponding to particular system parameters.

A three-to-one internal resonance $\omega_2 \cong 3\omega_1$ is considered for a range of rotation beam speed and it is assumed that there is no other commensurable frequency relationship with higher modes. The second natural frequency and three times the first natural frequency are plotted as functions of Ω in Figure 2. A three-to-one internal resonance is possible for a certain range of rotation speeds. The internal resonance is perfectly tuned when Ω is 326.82 rpm. The beam geometrical characteristics used are: L = 15 m, h = 0.3 m, b = 0.7 m, e = 0.05 m. The analyzed material is graphite-epoxy whose properties are E_1 = 144 GPa, E_2 = 9.65 GPa, G_{12} = 4.14 GPa, G_{13}=4.14 GPa, G_{23} = 3.45 GPa, ν_{12} = 0.3, ν_{13} = 0.3, ν_{23} = 0.5, for a sequence of lamination {*45/-45/-45/45*}. In this case, ρA= 138.9 Kg/m and EI = 9.81 10^7 Nm^2.

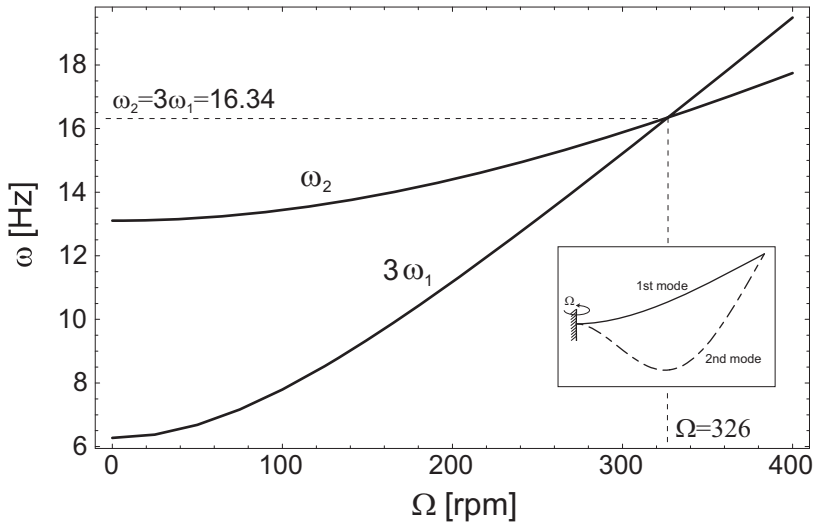

Figure 2. Variations of three times the first ω_1 and second ω_2 natural frequencies with the rotation speed Ω.

In this work, principal parametric resonance of first mode considering internal resonance is analyzed, involving the first two modes. Since none of these first two modes is in internal resonance with any other mode of the beam, all other modes except the directly or indirectly excited first or second mode decay with time due to the presence of damping and the first two modes will contribute to the long term system response (Nayfeh, 1996). Hence we can replace Eq. (25) by

$$
v_1(T_0,T_1,x)=A_1(T_1)\phi_1(x)e^{i\omega_1 T_0}+A_2(T_1)\phi_2(x)e^{i\omega_2 T_0}+cc, \tag{29}
$$

where *cc*. stands for the complex conjugate of the preceding terms and A_i are the unknown

complex-valued functions. In order to investigate the system response under internal and external resonance conditions, two detuning parameters σ_i are introduced:

$$\omega_2 = 3\omega_1 + \varepsilon\ \sigma_1, \quad \varpi = \omega_1 + \varepsilon\ \sigma_2. \tag{30}$$

Substituting Eqs. (29) and (30) to find the solution of Eq. (21), we get

$$D_0^2 v_2 + \alpha {v_2}^{iv} - \chi v_2'' + \lambda v_2' = \Gamma_1(T_1, x) e^{i\omega_1 T_0} + \Gamma_2(T_1, x) e^{i(3\omega_1 T_0 + \sigma_1 T_1)} + \frac{1}{2} f\ e^{i(\omega_1 T_0 + \sigma_1 T_2)} + cc + NST, \tag{31}$$

where the terms Γ_m are defined in Appendix. NST stands for terms that do not produce secular or small divisor terms. As the homogeneous part of Eq. (31) with its associated boundary conditions has a nontrivial solution, the corresponding nonhomogeneous problem has a solution only if a solvability condition is satisfied (Nayfeh and Mook, 1979). This requires the right-hand side of Eq. (31) to be orthogonal to every solution of the adjoint homogeneous problem, which leads to the following complex variable modulation equations for the amplitude and phase

$$2i\left(A_1' + \mu_1 A_1\right) + 8A_1\left(\gamma_{11} A_1 \bar{A}_1 + \gamma_{12} A_2 \bar{A}_2\right) + 8\delta_1 A_2 \bar{A}_1^{\,2} e^{i\sigma_1 T_1} - \frac{1}{2} f_1 e^{i\sigma_2 T_1} = 0, \tag{32}$$

$$2i\left(A_2' + \mu_2 A_2\right) + 8A_2\left(\gamma_{21} A_1 \bar{A}_1 + \gamma_{22} A_2 \bar{A}_2\right) + 8\delta_2 A_1^{\,3} e^{-i\sigma_1 T_1} = 0, \tag{33}$$

where prime denotes differentiation with respect to the slow time T_1 and μ_m, γ_m, δ_m and f_1 are defined in Appendix. Overbar indicates complex conjugate. The terms in the above equations involving the internal frequency detuning parameter σ_1 are the contributions of internal resonance in the system.

Introducing a Cartesian coordinates Eq. (34), the following amplitude and phase Eqs. (35-38) are finally obtained:

$$A_k = \frac{1}{2}\left[p_k(T_1) - i q_k(T_1)\right] e^{i\nu_k T_1} \qquad k = 1, 2. \tag{34}$$

$$p_1' = -\mu_1 p_1 - \nu_1 q_1 + \gamma_{11} q_1\left(p_1^{\,2} + q_1^{\,2}\right) + \gamma_{12} q_1\left(p_2^{\,2} + q_2^{\,2}\right) - \delta_1\left[2 p_1 q_1 p_2 - q_2\left(p_1^{\,2} + q_1^{\,2}\right)\right], \tag{35}$$

$$q_1' = -\mu_1 q_1 + \nu_1 p_1 - \gamma_{11} p_1\left(p_1^{\,2} + q_1^{\,2}\right) - \gamma_{12} p_1\left(p_2^{\,2} + q_2^{\,2}\right) - \delta_1\left[2 p_1 q_1 q_2 + p_2\left(p_1^{\,2} - q_1^{\,2}\right)\right] + \frac{1}{2} f_1, \tag{36}$$

$$p_2' = -\mu_2 p_2 - \nu_2 q_2 + \gamma_{21} q_2\left(p_1^{\,2} + q_1^{\,2}\right) + \gamma_{22} q_2\left(p_2^{\,2} + q_2^{\,2}\right) + \delta_2 q_1\left(3 p_1^{\,2} - q_1^{\,2}\right), \tag{37}$$

$$q_2' = -\mu_2 q_2 + \nu_2 p_2 - \gamma_{21} p_2\left(p_1^{\,2} + q_1^{\,2}\right) - \gamma_{22} p_2\left(p_2^{\,2} + q_2^{\,2}\right) + \delta_2 p_1\left(3 q_1^{\,2} - p_1^{\,2}\right), \tag{38}$$

where

$$\nu_1 = \sigma_2, \qquad \nu_2 = 3\sigma_2 - \sigma_1 \tag{39}$$

and the prime indicates the derivative with respect to T_1.

3 RESULTS AND DISCUSSION

For the analysis of the rotating beam subjected to principal parametric resonance of the first mode (i.e., $\varpi \cong \omega_1$) in presence of 3:1 internal resonance, system parameters are taken as mentioned earlier corresponding to the commensurable natural frequencies of the first and second mode of the system. There are no modal interactions involving other modes. The specific value of the rotating speed used for the study is Ω = 326.82 rpm for which ω_1 = 5.45 Hz and ω_2 = 16.35 Hz. The corresponding nonlinear interaction coefficients (defined in Eqs. (33 and 34)), for the specified rotating speed are: γ_{11} = 1.317, γ_{12} = 721.387, γ_{21} = -95.691, γ_{22} = -2256.731, δ_1 = -47.841 and δ_2 = 1.956.

3.1 Steady-state motions and stability

The equilibrium solutions of Eqs. (35-38) correspond to periodic motions of the beam. Steady-state solutions are determined by zeroing $p_i' = q_i' = 0$ the right-hand members of the modulation Eqs. (35-38) and solving the non-linear system. Stability analysis is then performed by analyzing the eigenvalues of the Jacobian matrix of the non-linear equations calculated at the fixed points. Amplitude-load curves are reported in Figures 3a and 3b, for external forces in a perfect resonance condition (σ_2 = 0) and for a small value of the external detuning parameter σ_2 = 0.2, respectively, considering damping $d_1 = d_2$ = 0.05 and internal detuning parameter σ_1 = 0.04. The amplitudes a_1 and a_2 are obtained by means of the following expression:

$$a_i = \sqrt{p_i^2 + q_i^2} \qquad i = 1,2. \tag{40}$$

In the case of σ_2 = 0.2 (Figure 3b), the modal solution branch alternatively loses and regains stability due to the presence of some saddle-nodes bifurcations.

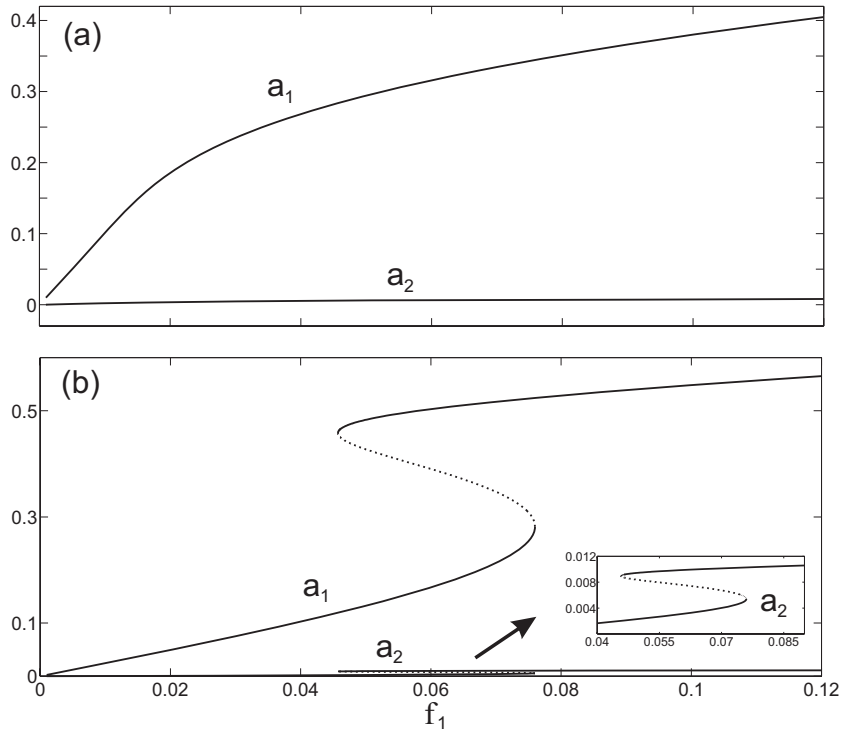

Figure 3. Amplitude-load curves: (a) Perfect external resonance σ_2 = 0; (b) External detuning parameter σ_2 = 0.2. Thick line: stable solutions; dashed line: unstable solutions.

The frequency-response curves are shown in Figures 4a and b, for an internal and external resonance condition. The modal amplitude a_i curves are obtained in function of the external detuning parameter σ_2. In this case, the forcing amplitude is f_1 = 0.05, modal damping d_i = 0.05 and internal detuning parameter σ_1= 0.04. The response curve corresponding to the first amplitude shows a noticeable hardening-spring type behavior (Figure 4a). The amplitude of the indirectly excited second mode is smaller in comparison with the first mode (Figure 4b). In the Figure 4, solid (dotted) lines denote stable (unstable) equilibrium solutions and thin solid lines denote unstable foci.

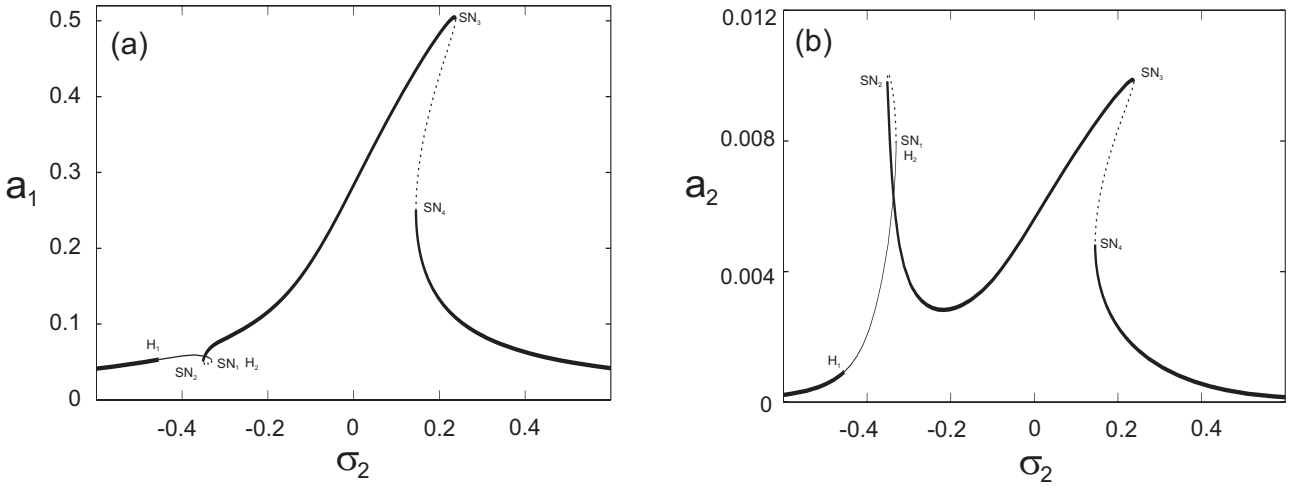

Figure 4. Frequency-response curves for: (a) first and (b) second modes, when f_1 = 0.05, σ_1 = 0.04 and d_i = 0.05. Solid (dotted) lines denote stable (unstable) equilibrium solutions and thin solid lines denote unstable foci.

The response curves exhibit an interesting behavior due to saddle-node bifurcations (where one of the corresponding eigenvalues crosses the imaginary axis along the real axis from the left- to the right-half plane) and Hopf bifurcations (where one pair of complex conjugate eigenvalues crosses the imaginary axis transversely from the left to the right-half plane). As σ_2 increases from a small value, the solution increases in amplitude and loses stability via a Hopf bifurcation at σ_2 = -0.4545 (H_1) and regains its stability via a reverse Hopf bifurcation at σ_2 = -0.3307 (H_2). Then, the response jumps to another branches of stable equilibrium solutions (jump effect), depending on the initial conditions. The dynamics solutions that emerge from this bifurcation will be analyzed in the next section. There is an unstable solution happening between two saddle-node bifurcations SN_1 and SN_2 (σ_2 = -0.3307 and σ_2 = -0.3516). The reduction in amplitude of the first mode represents an increased in the second mode amplitude. Increasing σ_2 beyond SN_2, the stable solution grows again in amplitude until arriving to a saddle-node bifurcation SN_3 (σ_2 =0.2378), resulting in a jump of the response to another branches of solutions. The new stable branch is left bounded by a saddle-node bifurcation SN_4 (σ_2 =0.1454).

When the modal damping is reduced d_i = 0.025, the influence of this effect is shown in Figures 5a and b, conserving the same forcing amplitude and internal detuning parameter values that the previous model. The frequency-response curves are similar to the previous case, and the modal amplitudes are larger. However, it can be seen that the influence of the first mode on the second mode response is smaller in the neighborhood of the Hopf bifurcation H_1 and the saddle-node SN_2.

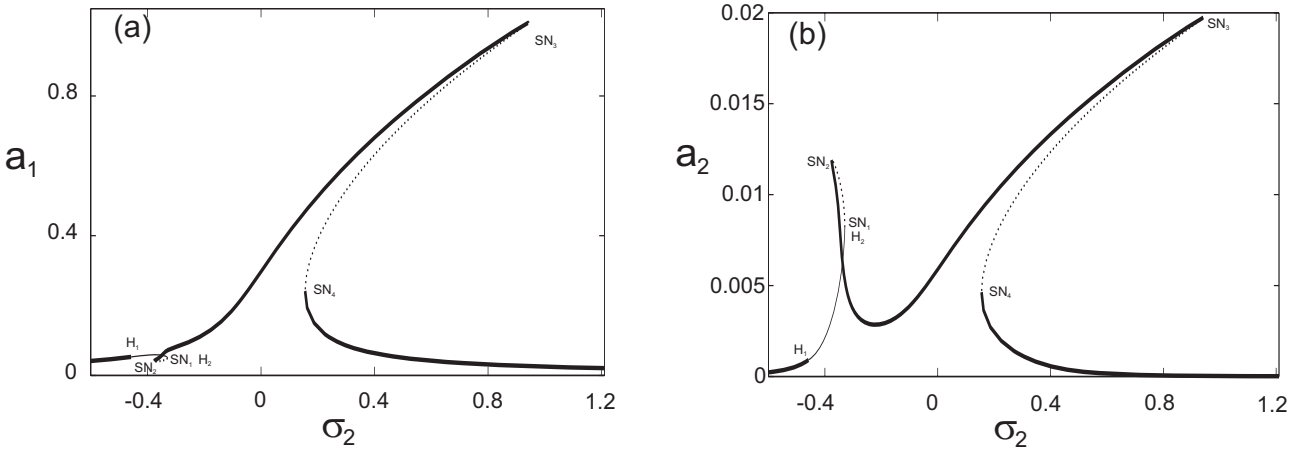

Figure 5. Frequency-response curves for: (a) first and (b) second modes, when $f_1 = 0.05$, $\sigma_1 = 0.04$ and $d_i = 0.025$. Solid (dotted) lines denote stable (unstable) equilibrium solutions and thin solid lines denote unstable foci.

The influence of the load amplitude parameter f_1 is on the frequency-response is analyzed in Figures 6a, b, c, d, e and f, where the modal damping considered is $d_i = 0.05$ and when the internal detuning parameter is far from the perfect resonance condition $\sigma_1 = 4$. When $f_1 = 0.1$ (Figures 6a and b), the frequency-response curves are similar to the previous case. However, for large values of σ_2 the stable equilibrium solution loses stability via a Hopf bifurcation at $\sigma_2 = 0.7318$ (H_3) and regains its stability via a reverse Hopf bifurcation at $\sigma_2 = 0.7834$ (H_4). The frequency-response curves for a forcing load $f_1 = 0.05$ is shown in Figures 6c and d, and for $f_1 = 0.025$ in Figures 6e and f. The amplitude of the second mode keeps almost the same when the load is reduced. However, as f_1 decreased, the dynamic behavior of the beam becomes more complicated and the hardening-spring curvature is also declining.

3.2 Dynamic solutions

According to the Hopf bifurcation theorem, small limit cycles are born as a result of the Hopf bifurcation. The born limit cycles are stable if the bifurcation is supercritical and unstable if the bifurcation is subcritical. Cycle-limit of the modulation equations correspond to aperiodic responses of the beam. In Figure 7, a schematic bifurcation diagrams for the orbits of the modulation Eqs. (35-38) in the neighborhood of the unstable foci when $f_1 = 0.05$, $\sigma_1 = 0.04$ and $d_i = 0.05$ (see Figure 4). The software XPP-AUTO (Doedel, 1997) is used to obtain the dynamic solutions that emerge from H_1. It is observed that a stable small limit cycle born due to the supercritical Hopf bifurcation at H_1 ($\sigma_2 = -0.4545$). Then, as σ_2 increases, the cycle limit grows and loses stability through a cyclic-fold bifurcation at CF_1 ($\sigma_2 = -0.4451$). Consequently, the two-period quasiperiod response of the beam jumps to another two-period quasiperiod response.

On the other hand, as σ_2 decreases past the supercritical Hopf bifurcation H_2 ($\sigma_2 = -0.3307$), the equilibrium solutions loses stability and gives way to a small-amplitude limit cycle. As the parameter σ_2 is reduced, the cycle limit loses and recovers stability through two cyclic-fold bifurcation CF_4 and CF_3 ($\sigma_2 = -0.3471$ and $\sigma_2 = -0.5063$, respectively). It is noticeable that subcritical instability exists. For example, between the interval $CF_3 < \sigma_2 < H_2$ and $CF_2 < \sigma_2 < H_1$ the beam response may be periodic or two-periodic quasiperiodic motion, depending on the initial conditions. When $H_1 < \sigma_2 < CF_1$ the beam response is a two period quasiperiodic motion.

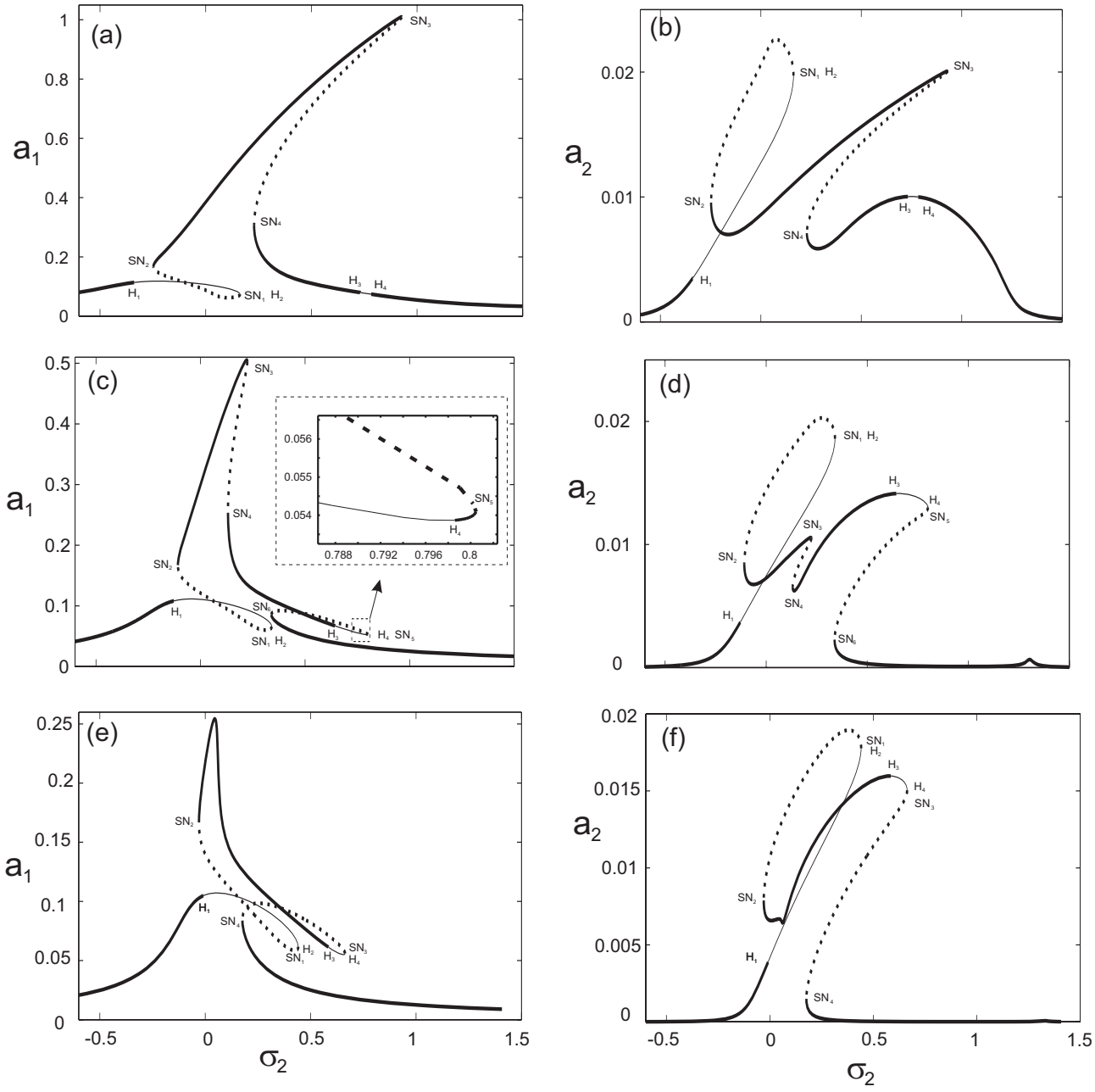

Figure 6. Frequency-response curves for the first and second modes when $d_i = 0.05$ and $\sigma_1 = 4$; (a,b) $f_1 = 0.1$, (c,d) $f_1 = 0.05$, (e,f) $f_1 = 0.025$. Solid (dotted) lines denote stable (unstable) equilibrium solutions and thin solid lines denote unstable foci.

As it was mention in the previous section, the dynamic behavior of the beam becomes more complicated for an internal detuning parameter $\sigma_1 = 4$ and for small values of the forcing amplitude f_1. The dynamic solutions for the case of $f_1 = 0.05$ and $d_i = 0.05$ are analyzed (according to the Figure 6b of frequency-response curves). In this case, there are four Hopf bifurcations, where H_1 ($\sigma_2 = -0.1284$) and H_4 ($\sigma_2 = 0.7989$) correspond to supercritical Hopf bifurcation, while H_2 ($\sigma_2 = 0.34056$) and H_3 ($\sigma_2 = 0.6437$) correspond to supercritical Hopf bifurcation. As σ_2 increases from the left Hopf bifurcation H_1, six branches of solutions are found in the neighborhood of H_1.

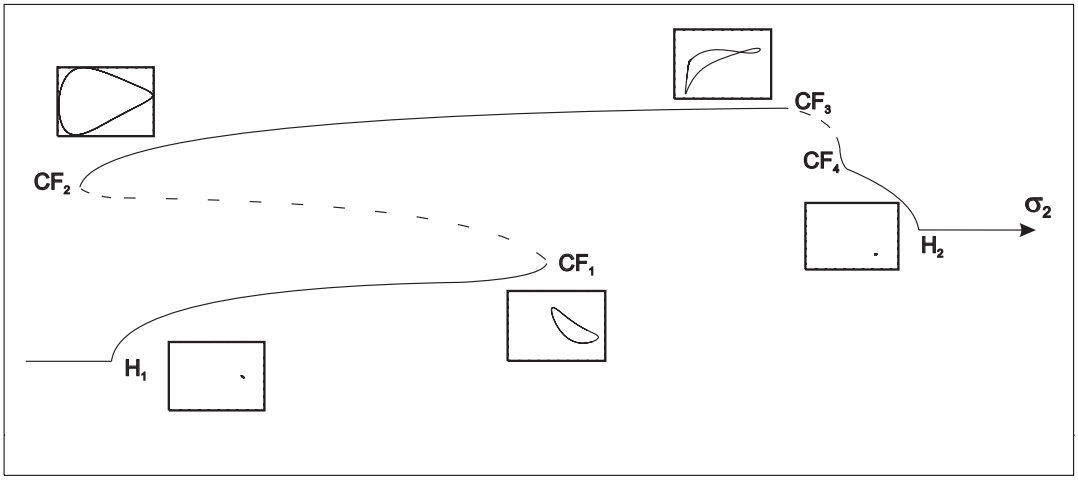

Figure 7. Schematic bifurcation diagrams illustrating the relative location of bifurcations, which limit cycle encounters between the Hopf bifurcation points when d_i = 0.05, σ_1 =0.0 4 and f_1 = 0.05. H = Hopf and CF = cycle-fold bifurcation.

A schematic diagram of these branches is shown in Figure 8. It is noticeable that multiple attractors coexist between these branches. The relative sizes of branches of cycles limit in the neighborhood of the Hopf bifurcation H_1 are: -0.1284 < σ_2 < -0.08 on branch I, -0.1421 < σ_2 < -0.14068 on branch II, -0.1571 < σ_2 < -0.1564 on branch III, -0.1716 < σ_2 < -0.17113 on branch IV, -0.1863 < σ_2 < -0.18598 on branch V, -0.2035 < σ_2 < -0.20324 on branch VI.

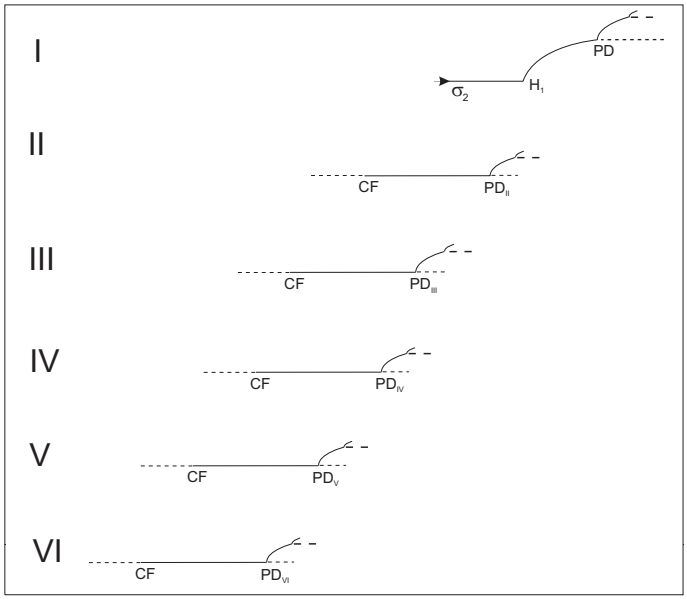

Figure 8. A schematic of the dynamic solutions found in the neighborhood of the Hopf bifurcation H_1, when d_i = 0.05, σ_1 = 4 and f_1 =0.05. H = Hopf bifurcation, CF = cycle-fold bifurcation and PD = period-doubling bifurcation.

In the first branch, a small limit cycle born as a result of the supercritical Hopf bifurcation H_1. Two-dimensional projections of the phase portraits of the limit cycle onto the p_1-p_2 plane at various pre and post-period-doubling bifurcation points are shown in Figures 9a-f. The period-one limit cycle (Figure 9a and b) grows and deforms and remains stable until a period-doubling bifurcation occurs PD_2 (σ_2 = -0.12470). Then it undergoes a sequence of period doubling bifurcations DP_4 (σ_2 = -0.12428190), DP_8 (σ_2 = -0.12420501), DP_{16} (σ_2 = -

0.12419385), culminating in a chaotic attractor as shown in Figure 10a (σ_2 = -0.12415). As σ_2 decreases slightly, the chaotic attractor increases in size and collides with its basin boundary, resulting in the destruction of the chaotic attractor and its basin boundary in a boundary crisis. As a result, the beam response jumps to a far away attractor, as it can be seen in the time history of p_1 in Figure 10b.

Two-dimensional projections of the phase portraits of the limit cycle found on branch II of Figure 8 are shown in Figure 11a. As σ_2 is increases, the limit cycle of period-1 grows and deforms and remains stable until a period-doubling bifurcation occurs. Then it undergoes a sequence of period doubling bifurcations, period-2 and period-4 (see Figure 11b and c), culminating in a chaotic attractor as shown in Figure 11d. The chaotic attractor keeps stable in size to σ_2 = -0.14068, after that value the response of the beam jumps to a periodic solution. The same dynamic behavior is observed in all the others branches. For example, period-doubling bifurcation occurs from the cycle limit which is found on branch III. Figures 12 a, b, c and d, show the two-dimensional projections of the phase portraits of the limit cycles onto the p_1-p_2 plane corresponding to different values of the internal detuning parameter σ_2. The chaotic attractor found in this branch disappear when σ_2 = - 0.1564 and the beam response jumps to a periodic solution, as in the previous branch.

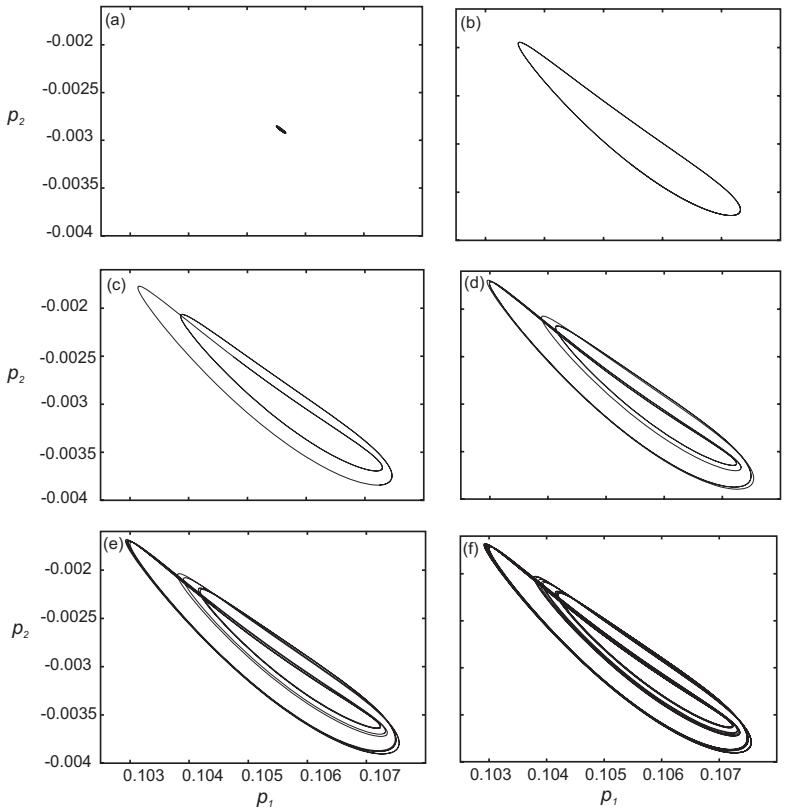

Figure 9. Two-dimensional projections of the phase portraits of the limit cycle found on branch I onto the p_1-p_2 plane, when d_i = 0.05, σ_1 = 4, f_1 =0.05 and σ_2 = (a) -0.1283 (p-1), σ_2 = (b) -0.1248 (p-1), σ_2 = (c) -0.1245 (p-2), σ_2 = (d) -0.12424 (p-4), σ_2 = (e) -0.12420 (p-8) and σ_2 = (d) -0.12419 (p-16).

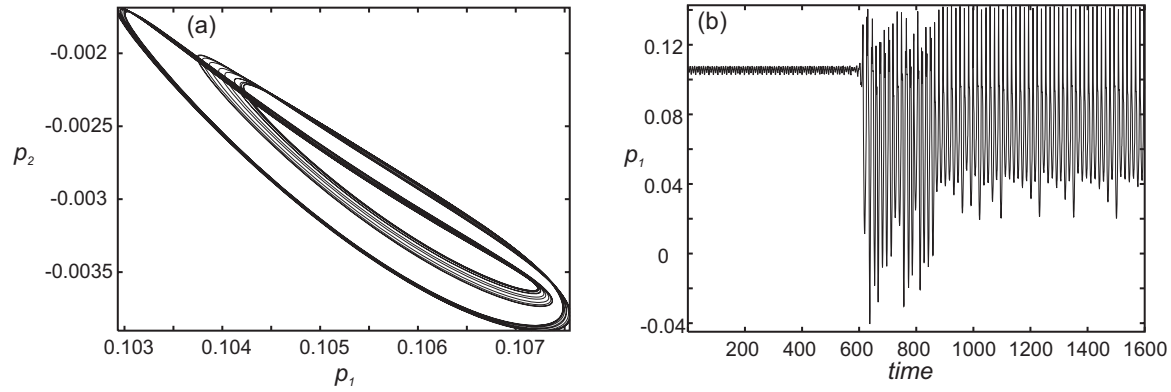

Figure 10. Attractor chaotic found in branch I, (a) two-dimensional projection of the phase portrait onto the p_1-p_2 plane for σ_2 = -0.12415, and (b) time history of p_1 after a crisis had occurred for σ_2 = -0.10215.

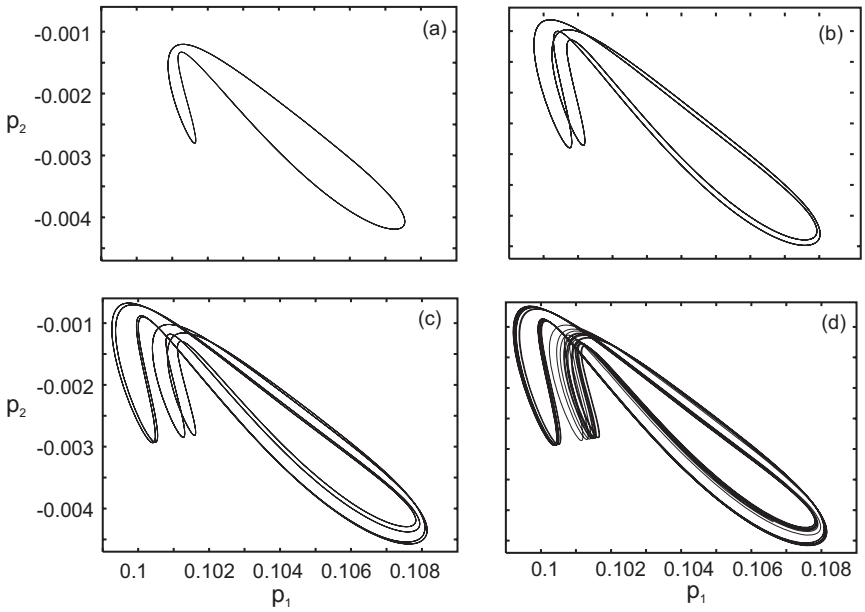

Figure 11. Two-dimensional projections of the phase portraits of the limit cycle found on branch II onto the p_1-p_2 plane, when σ_2 = (a) -0.141819 (p-1), σ_2 = (b) -0.140955 (p-2), σ_2 = (c) -0.14075 (p-4), σ_2 = (d) -0.1473 (attractor).

The limit cycle of period-1 corresponding to branch IV is shown in Figure 13a. As σ_2 is increases, period doubling bifurcations are also found on this branch. The limit cycles of period-2 and 4 are shown in Figure 13b and c. The chaotic attractor found at σ_2 = -0.17117 is shown in Figure 13d, and it remains alive until σ_2 = -0.17113.

A cycle-fold bifurcation occurs at the left end of the branch V (see Figure 8), whereas a one supercritical period-doubling bifurcation appears to the right when the σ_2 is increases. The limit cycles calculated on this branch are shown in Figure 14a, b and c. A chaotic attractor is found at σ_2 = -0.186001 (Figure 14d) and it is valid until the beam response jumps to a periodic solution when σ_2 is increased to -0.18598. As in the previous branches, the two-dimensional projections of the phase portraits of the limit cycle found on the last branch VI of Figure 8 are shown in Figure 15a, b and c. The chaotic attractor size found on this branch is a little larger in comparison with those found on the others branches.

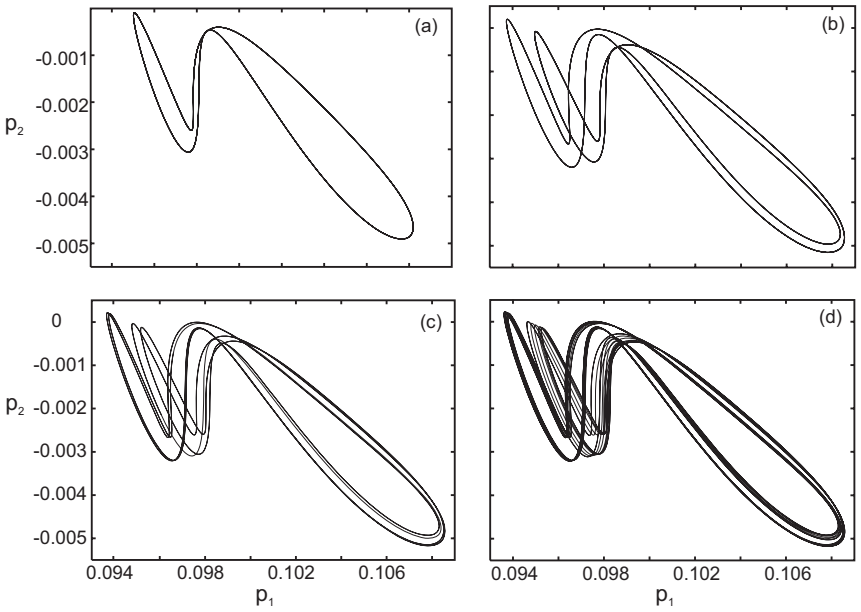

Figure 12. Two-dimensional projections of the phase portraits of the limit cycle found on branch III onto the p_1-p_2 plane, when σ_2 = (a) -0.156966 (p-1), σ_2 = (b) -0.15655 (p-2), σ_2 = (c) -0.156465 (p-4), σ_2 = (d) -0.15646 (attractor).

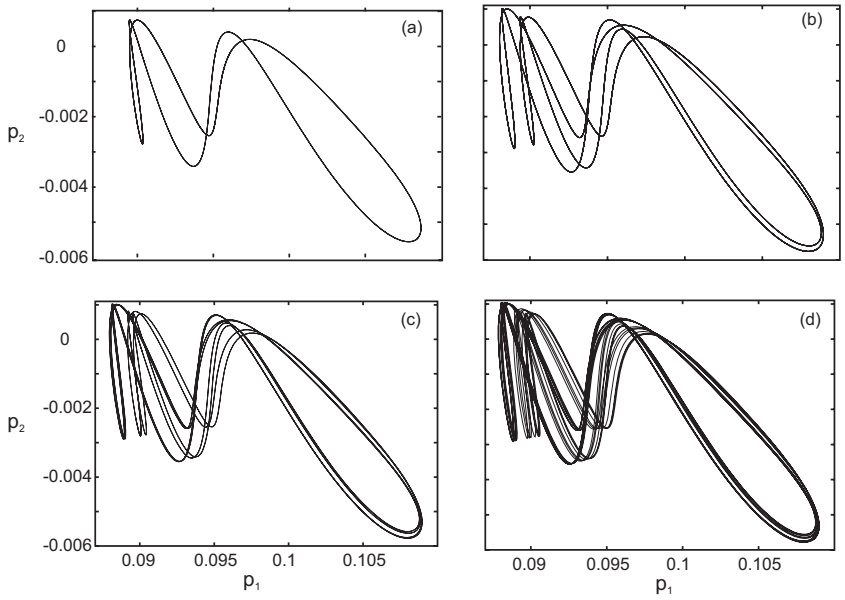

Figure 13. Two-dimensional projections of the phase portraits of the limit cycle found on branch IV onto the p_1-p_2 plane, when σ_2 = (a) -0.171515 (p-1), σ_2 = (b) -0.1712011 (p-2), σ_2 = (c) -0.171189 (p-4), σ_2 = (d) -0.17117 (attractor).

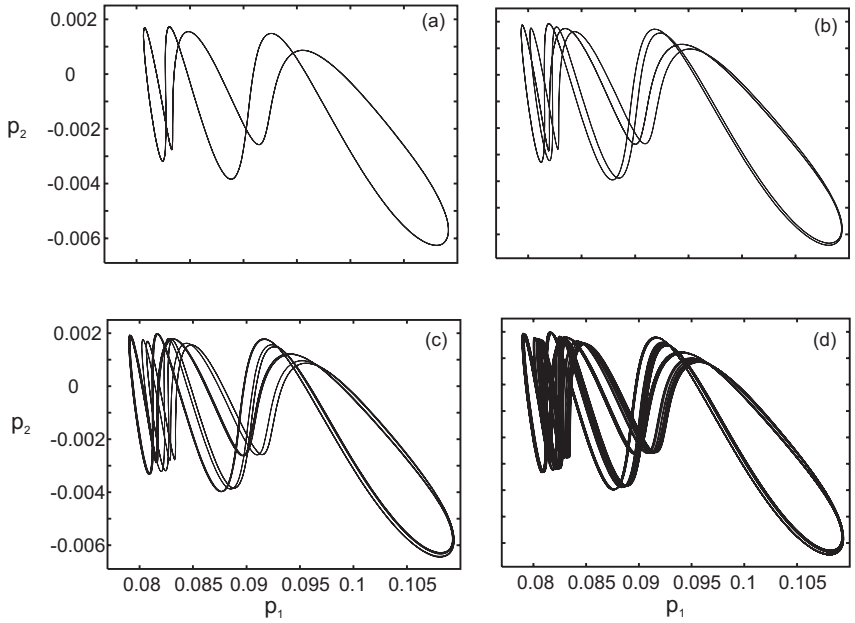

Figure 14. Two-dimensional projections of the phase portraits of the limit cycle found on branch V onto the p_1-p_2 plane, when σ_2 = (a) -0.1862268 (p-1), σ_2 = (b) -0.1862264 (p-2), σ_2 = (c) -0.1860081 (p-4), σ_2 = (d) -0.186001 (attractor).

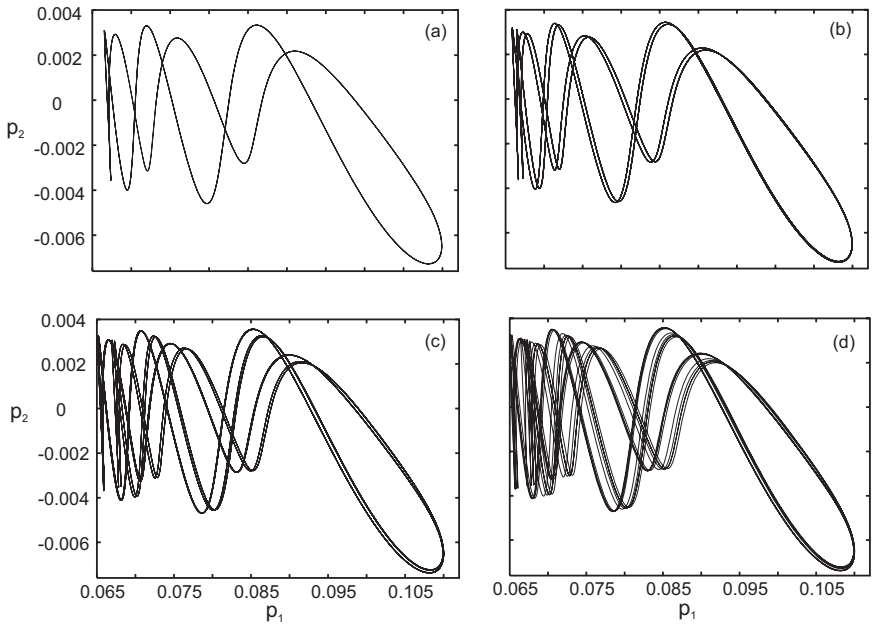

Figure 15. Two-dimensional projections of the phase portraits of the limit cycle found on branch VI onto the p_1-p_2 plane, when σ_2 = (a) -0.2033020 (p-1), σ_2 = (b) -0.20331951 (p-2), σ_2 = (c) -0.203270 (p-4), σ_2 = (d) -0.203250 (attractor).

On the other hand, there is another supercritical Hopf bifurcation denoted as H_4 (σ_2 = 0.7989) in the frequency-response of Figure 8. In this case, when σ_2 decreases from the right Hopf bifurcation H_4, two branches of solutions are found in the neighborhood of H_4. A schematic diagram of these branches is shown in Figure 16. It is supposed that some attractors can coexist as in the previous case. The relative sizes of branches of cycles limit in the neighborhood of the Hopf bifurcation H_4 are: $0.795 < \sigma_2 < 0.7984$ on branch I, and $0.1421 < \sigma_2 < -0.14068$ on branch II.

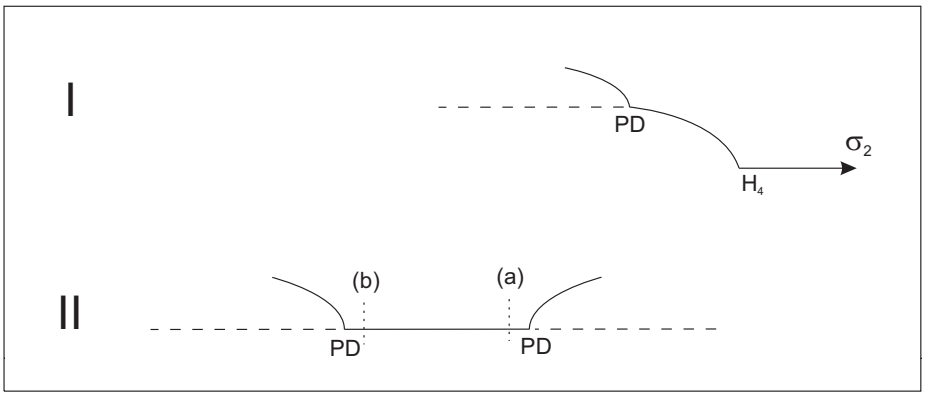

Figure 16. A schematic of the dynamic solutions found in the neighborhood of the Hopf bifurcation H_4, when d_i = 0.05, σ_1 = 4 and f_1 =0.05. H = Hopf bifurcation and PD= period-doubling bifurcation.

In Figure 17a, it is shown a two-dimensional projection of the phase portrait of the limit cycle born as decreases σ_2 past H_4 on branch I. As σ_2 decreases further, the limit cycle grows and deforms as shown in Figure 17b. Then, the deformed limit cycle undergoes a sequence of supercritical period-doubling bifurcations, leading to chaos. Figures 17c, d and e, shown the representative period-2, period-4 and period-8 limit cycles. The representative chaotic attractor at σ_2 = 0.79637 is shown in Figure 16f. Decreasing σ_2 the beam response jumps from the large chaotic amplitude to a small periodic solution when σ_2 = - 0.795.

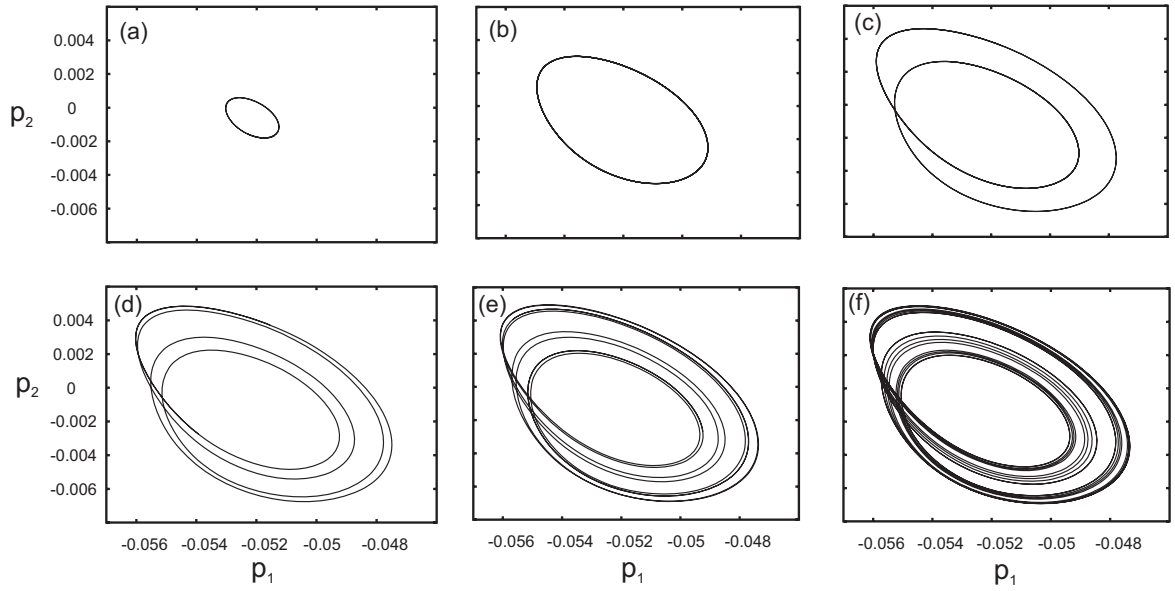

Figure 17. Two-dimensional projections of the phase portraits of the limit cycle found on branch I onto the p_1-p_2 plane, from H_4, when σ_2 = (a) 0.7986741 (p-1), σ_2 = (b) 0.797558 (p-1), σ_2 = (c) 0.7965944 (p-2), σ_2 = (d) 0.796467 (p-4), σ_2 = (e) 0.79638778 (p-8), σ_2 = (f) 0.79637 (attractor).

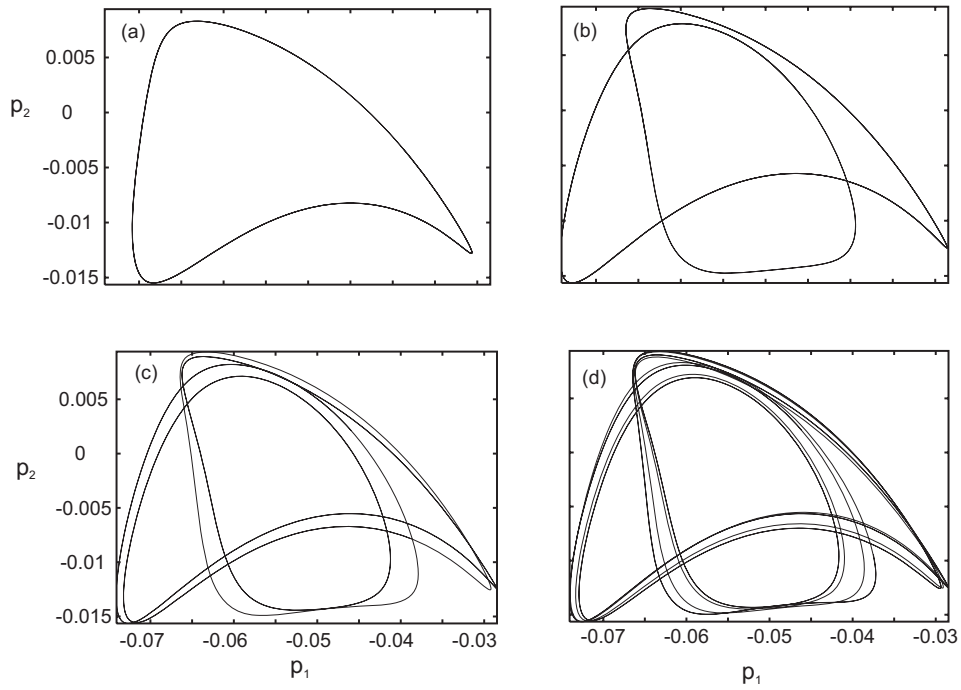

Figure 18. Two-dimensional projections of the phase portraits of the limit cycles found to the right side on branch II onto the p_1-p_2 plane, when σ_2 = (a) 0.76319 (p-1), σ_2 = (b) 0.7653290 (p-2), σ_2 = (c) 0.7658692 (p-4), σ_2 = (d) 0.76596581 (p-8).

Two sequences of supercritical period-doubling bifurcations are found on branch II, corresponding to σ_2 = 0.74399 to the left and σ_2 = 0.7636 to the right of the schematic Figure 16. Two-dimensional projections of the phase portraits of the limit cycle onto the p_1-p_2 plane at pre period-doubling bifurcation right point, stated with (a) in Figure 16, is shown in Figure 18a. As σ_2 increases, the limit cycle undergoes a sequence of supercritical period-doubling bifurcations, leading to chaos. Some of the limit cycles of period-2, -4 and -8 are shown in Figure 18b, c and d, respectively. On the left side of the branch II, a period-1 limit cycle is shown in Figure 19a corresponding to the σ_2 setting state with (b) in Figure 16. As σ_2 decreases, the limit cycle found a supercritical period-doubling bifurcation. Then the period-2 cycle limit (see Figure 19 b) remains stable until it encounters a cycle fold bifurcation at σ_2 = 0.742966895.

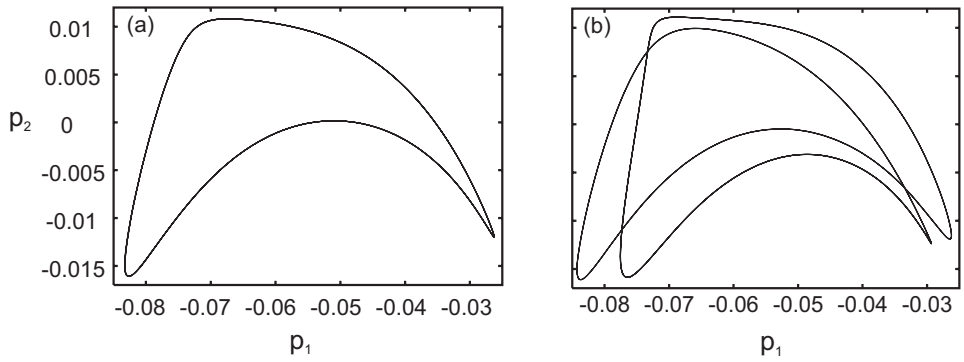

Figure 19. Two-dimensional projections of the phase portraits of the limit cycles found to the left side on branch II when σ_2 = (a) 0.744328 (p-1), σ_2 = (b) 0.7429668 (p-2).

4 CONCLUSIONS

The nonlinear planar response of a cantilever rotating box beam to a principal parametric resonance of its first flexural mode is investigated. The beam is subjected to a harmonic transverse load in the presence of internal resonance. The internal resonance can be activated for a range of the beam rotating speed, where the second natural frequency is approximately three times the first natural frequency. Geometric cubic nonlinear terms are included in the equation of motion due to midline stretching of the beam. The material is considered to be linear elastic and the cross-section properties are assumed to be constant given the assumption of small strains.

By means of the method of multiple scales applied directly on the partial-differential equation four first-order nonlinear ordinary-differential equations were derived, describing the modulation of the amplitudes and phases of the interacting modes. The resonant behavior is illustrated by frequency-response and amplitude-load curves for a sequence of lamination of {*45/-45/-45/45*}. The curves are generated using a pseudo arclength continuation scheme. Calculating the eigenvalues of the Jacobian matrix, the stability of these responses is assessed. The frequency-response curves exhibit a hardening type behavior. When the excitation frequency is slowly varied, the response may undergo saddle-node and Hopf bifurcations. On the other hand, when the internal detuning parameter is varied from its perfect condition, the frequency-response curves exhibit a more complex behavior. It was shown that this effect is also influenced by the decrease of the load amplitude parameter value. In this case, it was found that the modulation equations posses complex dynamics, including supercritical period-doubling bifurcation, the coexistence of multiple attractors, and various jump responses driven by cyclic-fold bifurcation, subcritical period-doubling bifurcations, and boundary crises. The limit cycle solutions of the modulation equations may undergo a sequence of period-doubling bifurcations, culminating in chaos. The chaotic attractors may undergo attracting-merging and boundary crises.

ACKNOWLEDGEMENTS

The present study was sponsored by Secretaría de Ciencia y Tecnología, Universidad Tecnológica Nacional, and by CONICET.

REFERENCES

Apiwattanalunggarn, P., Shaw, S.W., Pierre, C., and Jiang, D., Finite-Element-Based Nonlinear Modal Reduction of a Rotating Beam with Large-Amplitude Motion. *Journal of Vibration and Control* 2003 9: 235.

Barbero, E.J., *Introduction to Composite Material Design*. Taylor and Francis Inc, 1999.

Doedel E.J., A*UTO97 Continuation and bifurcation software for ordinary differential equations*, Available by anonymous ftp from FTP.CS.CONCORDIA.CA, directory PUB/DOEDEL/AUTO1997.

Hodges D.H., and Rutkowski, M.J., Free-vibration analysis of rotating beams by a variable-order finite-element method. *AIAA Journal*, 19:1459-1466, 1981.

Leissa, A., Vibrational aspects of rotating turbomachinery blades. *ASME Applied Mechanics Reviews*, 34:629-635, 1981.

Librescu, L., *Thin –Walled Composite Beams*¸ Springer, Dordrecht, 2006

Machado, S.P., Filipich, C.P., and Cortínez, V.H., Parametric vibration of thin-walled composite beams with shear deformation. *Journal of Sound andVibration* 305:563–581, 2007.

Nayfeh A.H., J.F. Nayfeh, D.T. Mook, On methods for continuous systems with quadratic and cubic nonlinearities, Nonlinear Dynamics 3:145–162, 1992.

Nayfeh, A.H., and Mook, D.T., *Nonlinear Oscillations*, Wiley, 1979.

Nayfeh, A.H., and Balachandran B., Modal interactions in dynamical and structural systems, *Applied Mechanics Reviews*, 42:175-201, 1989.

Nayfeh, A.H., and Balachandran B., *Applied Nonlinear Dynamics: analytical computational and Experimental Methods*, Wiley-Interscience, 1995.

Nayfeh, A.H., *Nonlinear Interactions*, Wiley, 1996.

Pesheck, E., Pierre, C., and Shaw, S. W., Accurate reduced order models for a simple rotor blade model using nonlinear normal modes. *Mathematical and Computer Modeling*, 33:1085–1097, 2001.

Pesheck, E., Pierre, C., and Shaw, S.W., Modal reduction of a nonlinear rotating beam through nonlinear normal modes. *ASME Journal of Vibration and Acoustics*, 124:229–236, 2002a,

Pesheck, E., Pierre, C., and Shaw, S.W., A new Galerkin-based approach for accurate nonlinear normal modes through invariant manifolds. *Journal of Sound and Vibration*, 249:971–993, 2002b.

Schilhansl, M.J., Bending frequency of a rotating cantilever beam. *ASME Journal of Applied Mechanics*, 25:28-30, 1958.

Shaw, S.W. and Pierre, C., Normal modes for non-linear vibratory systems. *Journal of Sound and Vibration*, 164:85–124, 1993.

Shaw, S.W., and Pierre, C., Normal modes of vibration for non-linear continuous systems. *Journal of Sound and Vibration*, 169:319–347, 1994.

Shaw, S.W., Pierre, C., and Pesheck, E., Modal analysis-based reduced-order models for nonlinear structures-an invariant manifold approach. *The Shock and Vibration Digest*, 31:3–16, 1999

Turhan, O., and Bulut, G., On nonlinear vibrations of a rotating beam. *Journal of Sound and Vibration*, 322:314–335, 2009.

Wang, J.T.S., Mahrenholtz, O., and Bohm, J., Extended Galerkin's method for rotating beam vibrations using Legendre polynomials. *Solid Mechanics Archives*, 1:341-365, 1976.

APPENDIX

The terms used in the Eqs. (31), (32) amd (33) are defined as:

$$\Gamma_1 = -2i\omega_1\phi_1\left(A_1' + \mu A_1\right) + \left(3\phi_1''\int_0^1 \phi_1'^2 dx\right)A_1^2\bar{A}_1 + \left(2\phi_1''\int_0^1 \phi_1'\phi_2' dx + \phi_2''\int_0^1 \phi_1'^2 dx\right)A_2\bar{A}_1^2 e^{i\sigma_1 T_1} + \left(4\phi_2''\int_0^1 \phi_1'\phi_2' dx + 2\phi_1''\int_0^1 \phi_2'^2 dx\right)A_1A_2\bar{A}_2, \tag{41}$$

$$\Gamma_2 = -2i\omega_2\phi_2\left(A_2' + \mu A_2\right) + \left(3\phi_2''\int_0^1 \phi_2'^2 dx\right)A_2^2\bar{A}_2 + \left(\phi_1''\int_0^1 \phi_1'^2 dx\right)A_1^3 e^{-i\sigma_1 T_1} + \left(4\phi_1''\int_0^1 \phi_1'\phi_2' dx + 2\phi_2''\int_0^1 \phi_1'^2 dx\right)A_1A_2\bar{A}_1, \tag{42}$$

$$\mu_m = \int_0^1 \mu(x)\phi_m{}^2 dx \tag{43}$$

$$\gamma_{mm} = \frac{3}{8\omega_m}\Gamma_{mmmm} \tag{44}$$

$$\gamma_{mn} = \frac{1}{8\omega_m}\left(4\Gamma_{mmnn} + 2\Gamma_{mmnn}\right), \quad m \neq n \tag{45}$$

$$\delta_1 = \frac{1}{8\omega_1}\left(2\Gamma_{1112} + \Gamma_{1211}\right), \tag{46}$$

$$\delta_2 = \frac{\Gamma_{2111}}{8\omega_2}, \tag{47}$$

$$\Gamma_{mnpq} = -\left(\int_0^1 \phi_m \phi_n'' dx\right)\left(\int_0^1 \phi_p' \phi_q' dx\right), \tag{48}$$

$$f_m = \frac{1}{\omega_m}\int_0^1 f(x)\phi_m dx \tag{49}$$